On the Sensitivity to Height and Motion of Bistatic SAR Interferometry
A Spectral View

Theodosiou, Andreas; López-Dekker, Paco

DOI
10.1109/TGRS.2024.3399598

Publication date
2024

Document Version
Final published version

Published in
IEEE Transactions on Geoscience and Remote Sensing

On the Sensitivity to Height and Motion of Bistatic SAR Interferometry: A Spectral View

Andreas Theodosiou and Paco López-Dekker, *Senior Member, IEEE*

***Abstract*— Assessing the performance of interferometers and processing interferograms require accurate knowledge of the temporal lag, sensitivity, and spectral shift. While these parameters are well-defined for conventional interferometric configurations, their definition becomes opaque for complex configurations, such as bistatic systems with formation-flying satellites. According to the principle of diffraction tomography, each instrument samples a distinct region of the scattering surface's Fourier domain. Using this principle, we introduce a wavenumber-domain method for calculating the temporal lag, spectral shift, and sensitivity to height of synthetic-aperture radar (SAR) interferometers. The method calculates interferometric parameters by aligning the ground-projected wavenumber support of the SAR images forming the interferogram. Although the wavenumber-support method agrees with the conventional geometric formulations of the temporal lag and sensitivity in geometrically simple cases, the two methods diverge in more complex geometries. We show that when the two SAR satellites fly in a close-formation or have lines of sight that are squinted with respect to the zero-Doppler direction, then the geometric formulations are inadequate and the wavenumber-support method is needed to accurately estimate the interferometric parameters.**

***Index Terms*— Bistatic synthetic-aperture radar (SAR), bistatic SAR interferometry, diffraction tomography, formation flying, InSAR, interferometry, line of sight, multistatic SAR, SAR, spectral support, squint, squinted geometry.**

I. Introduction

WHAT is the temporal lag and the height sensitivity of a synthetic-aperture radar (SAR) interferometer? Scientists familiar with the instrument would consider the answer obvious. When the instrument's look direction is perpendicular to the flight direction, these two parameters are proportional to the projections of the antennas' physical separation in the relevant directions. For example, an along-track interferometer (ATI) with two antennas on a single platform has a temporal lag directly proportional to the along-track separation [1], [2], [3]. Similarly, a cross-track interferometer (XTI) with sensors that are only separated in the plane normal to the flight direction has a sensitivity proportional to the baseline of the two antennas perpendicular to the line of sight [4], [5].

Manuscript received 13 November 2023; revised 27 March 2024; accepted 1 May 2024. Date of publication 9 May 2024; date of current version 23 May 2024. This work was supported by the European Space Agency (ESA) through the Harmony Phase-A Science Consolidation Studies under ESA under Grant 4000134959/21/NL. *(Corresponding author: Andreas Theodosiou.)*

The authors are with the Department of Geoscience and Remote Sensing, Delft University of Technology, 2628 Delft, The Netherlands (e-mail: a.theodosiou@tudelft.nl).

Digital Object Identifier 10.1109/TGRS.2024.3399598

The link between interferometric parameters, namely height sensitivity and temporal lag, and geometric parameters stems from a geometric approach to interferometry. The geometric approach relates the phase of an interferogram to, in the case of XTI, the elevation of the surface, and the case of ATI to the radial motion of the surface. This approach hinges on the assumption that the SAR signal is monochromatic. In other words, it assumes that the signal bandwidth in range and azimuth is small enough to be considered negligible. The monochromatic assumption hides the role that the ground reflectivity spectrum plays in interferometry. Gatelli explained the implications of considering the ground-range wavenumber shift for a conventional XTI [6]. One that has separation only perpendicular to the line of sight. This has led to the introduction of spectral shift filtering in the processing of interferograms [6], [7], [8].

Nevertheless, the monochromatic approach remains the primary view of interferometry, if for no other reason than that it is intuitive. The approach and consequently the geometric methods of calculating interferometric parameters, while intuitive, break down in more complex geometries. Consider an interferometer operating bistatically with a squinted line of sight, for example, a system similar to TanDEM-X [9] or Harmony [10]. The time taken for the lagging phase center to *see* a given point on the surface with the same viewing geometry as the leading phase center is not a the function of the along-track separation alone. Hence, the temporal lag is not equal to half the tangential separation of the phase centers, as is the case for bistatic interferometers with a line of sight perpendicular to the flight direction.

Likewise, since the bistatic lines of sight do not share a common radial–normal plane, they first need to be aligned before calculating the perpendicular baseline, which drives the geometric expression of the sensitivity. However, the lines of sight of the two sensors do not necessarily align during the illumination time of a given point, since the transmitter–receiver pairs have a bistatic line of sight with a common ending point but different starting points and different directions. Thus, applying the geometric method is not possible.

Employing the monostatic equivalent (ME) of each transmitter–receiver pair [11] provides a workaround to this problem and allows one to geometrically compute the interferometric baselines. Nevertheless, the location of the ME of a system that has a 3-D separation and squinted line of sight becomes complicated. A different ME exists for each combination of slow time and look angle, as Fig. 1 shows.

In this article, we present a more accurate method for solving this problem. The fundamental relation of diffraction

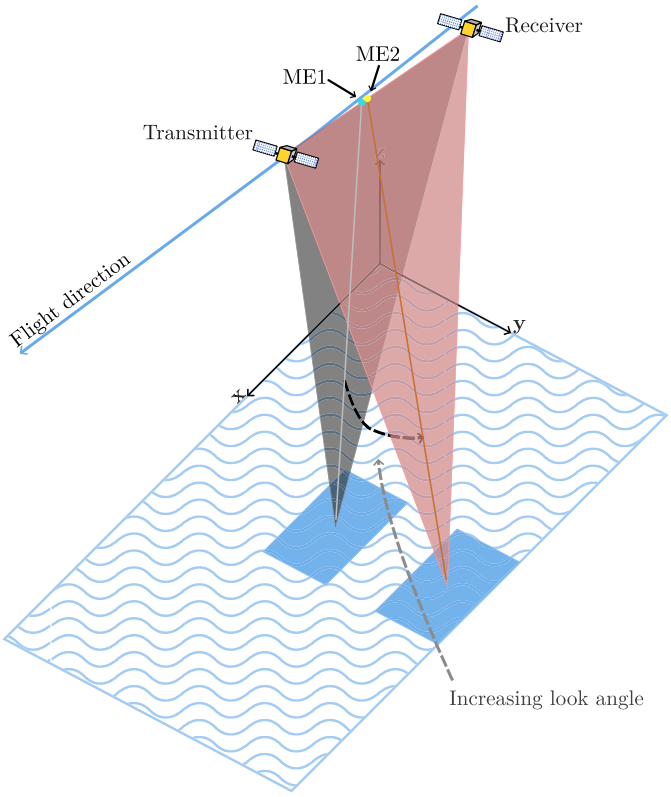

Fig. 1. Locations of the MEs for a given slow time and two different look angles. As the look angle increases, the location of the ME shifts along the line segment connecting the transmitter to the receiver. Thus, the ME system does not have a single location for a given slow time, as a true monostatic system would.

tomography states that the field scattered by an object is directly proportional to the object function's Fourier transform at the wavenumbers that correspond to the incident and scattered wave vectors. Building on this idea, we propose using the wavenumber support of the two SAR images to calculate these interferometric parameters. In Sections II–IV, we show that by finding the temporal and spectral shifts that align the wavenumber supports of the two sensors, we can calculate the temporal lag and the interferometer sensitivity. Our technique applies to all interferometers, monostatic and bistatic, with temporally varying or fixed separations, regardless of squint.

II. Spectral Approach to SAR Interferometry

A. Fundamental Relation of Diffraction Tomography

Before delving into interferometry, we will first motivate our wavenumber-domain approach by linking the fundamental principle of diffraction tomography to the region of support, that is, the subset of the image domain that maps to nonzero values, of a SAR image. Consider an instrument illuminating an object, with complex reflectivity $o(\boldsymbol{r_s})$ where $\boldsymbol{r_s}$ represents the position vector, with a monochromatic electromagnetic wave. A second the instrument, receives the scattered electromagnetic wave. Assuming that the object is homogeneous, that the Born approximation is valid, and neglecting geometric attenuation, the received field is [12]

$$u(\boldsymbol{r_T}, \boldsymbol{r_R}) = \iiint_V o(\boldsymbol{r}'_s) e^{-jk_0(R_T(\boldsymbol{r_T}, \boldsymbol{r}'_s) + R_R(\boldsymbol{r_R}, \boldsymbol{r}'_s))} \, \mathrm{d}\boldsymbol{r}'_s \tag{1}$$

where $\boldsymbol{r_T}, \boldsymbol{r_R}$ are the positions of the transmitter and the receiver, respectively, R_T, R_R are the distances to the object from the transmitter and the receiver, respectively, and the integration is taken over the volume of the object.

We now consider a small neighborhood around the object at $\boldsymbol{r_0}$ and carry out the first-order Taylor expansion of the distances for a given position of the transmitter and the receiver. The expansion yields the well-known plane wave approximation of spherical waves

$$R_n(\boldsymbol{r_n}, \boldsymbol{r_s}) \approx R_n(\boldsymbol{r_0}) + \nabla R_n(\boldsymbol{r_0}) \cdot (\boldsymbol{r_s} - \boldsymbol{r_0}) \tag{2}$$

where the subscript n can be either T or R. ∇R_n is the gradient of the slant range and since R_n represents the distance along a spherical wave, the gradient points in the line of sight direction. For a typical SAR satellite in a low-Earth orbit, such as Sentinel-1, with altitude 693 km, a look angle of 26°, assuming a rectilinear geometry, and setting $\boldsymbol{r_s} = (10\text{ m}, 2.5\text{ m}, 0\text{ m})^T$ to correspond to half a resolution cell, the relative error between the expansion in (2) and the true slant range is 8.8×10^{-9} %. Hence, from this point on, we proceed with our analysis using the plane wave approximation.

Substituting (2) into (1), and moving the constant phase terms out of the integral, we note that the volume integral becomes the 3-D Fourier transform of the scattering density $\tilde{o}$ [13]

$$u(\boldsymbol{r_T}, \boldsymbol{r_R}) \approx \tilde{o}(\boldsymbol{k_T} + \boldsymbol{k_R}) \tag{3}$$

where $\boldsymbol{k_T} = k_0 \nabla R_T(\boldsymbol{r_0})$ and $\boldsymbol{k_R} = k_0 \nabla R_R(\boldsymbol{r_0})$ are the transmitter and receiver wave vectors, respectively, and we have neglected the leading phase term. This is the fundamental principle of diffraction tomography [13], [14]. Equation (3) states that the received field is proportional to the Fourier transform of the illuminated object at the components of the total wave vector, $\boldsymbol{k_T} + \boldsymbol{k_R}$. The result demonstrates that the instrument samples the Fourier space of the object's reflectivity at one point in the spatial frequency domain [15]. The line of sight of the instrument and the carrier wavelength determine the point in the spatial frequency domain at which the object is sampled. By varying the viewing geometry, for example, moving the location of the transmitter and receiver, or changing the look and squint angles of the antennas, the instrument can sample different points of the Fourier domain.

A SAR samples the scattered electromagnetic field with a certain impulse response. Thus, the signal of the SAR image becomes [4]

$$u(x, \eta) = e^{-jk_0 R_0} (f * \chi)(x, \eta) \tag{4}$$

where $*$ denotes the linear 2-D convolution, $R_0 = R_T(\boldsymbol{r_0}) + R_R(\boldsymbol{r_0})$, and we have used the range coordinate, η, and the azimuth coordinate, x, as the image coordinates, and the elevation, ζ, which is perpendicular to both as the third axis. In this expression, we have assumed that setting the azimuth position sets the positions of the receiver and the transmitter. $\chi(x, \eta)$ is the system impulse response, and we have defined the following symbol for brevity:

$$f(x, \eta) = e^{-j\boldsymbol{k}\cdot\boldsymbol{r_s}} \int_Z o(\boldsymbol{r_s}) \, \mathrm{d}\zeta. \tag{5}$$

The plane wave exponential has been moved out of the integral because any component of $\boldsymbol{r_s}$ along the elevation

direction will, by definition, be perpendicular to the wave vector. Additionally, the system impulse response does not depend on the elevation, since it is perpendicular to the plane of the SAR image. Consequently, the integral with respect to elevation only contains the object's reflectivity. It represents the projection of the scattering object onto the range and azimuth axes. Thus, each sample in a SAR image is a single tomographic projection of the scattering object, shifted by the plane wave exponential and filtered by the instrument's impulse response [4].

SARs do not transmit and receive monochromatic waves. On the contrary, they use chirp waveforms that have a certain bandwidth. Therefore, with each pulse, the radar samples the Fourier domain of the object along the line $k_0(f_r)(\nabla R_T(\boldsymbol{r_0}) + \nabla R_R(\boldsymbol{r_0}))$, where $k_0(f_r)$ is the instantaneous wavenumber that corresponds to the frequency f_r of the chirp signal. Acquiring a second SAR image, from a different position, produces a different tomographic projection of the scattering object. Cross-track interferometry uses these two different projections of the scattering object to infer the relative height of the scatterer.

B. Mathematical Derivation of the Spectral Shift in Two Dimensions

The fundamental principle of the method discussed in this article is that only the energy that comes from the wavenumbers that coincide between the two images contributes to the interferometric signal. In cases where the wavenumber supports of the two images are disjoint, the interferometric signal drops to zero. Therefore, forming an interferogram aligns the wavenumber supports of the two images, and the temporal lag and wavenumber shifts correspond to the moment where the wavenumber supports of the two images are aligned. Prati and Rocca [8] first proved this for the range wavenumbers and for an interferometer that has only a perpendicular separation. Gatelli et al. [6] expanded on the spectral shift due to different look angles and on its exploitation for the improvement of interferometric techniques. The idea that only the overlapping parts of the spectra in two dimensions, in range and azimuth, contribute to interferometric information has also been used in [16] to correct for the large angle between acquisitions coming from satellites that followed crossing orbits. In this section, we provide a derivation of this principle in two dimensions, range, and azimuth, for a bistatic interferometer with an arbitrary separation between the two SARs that compose it.

Consider an XTI where two bistatic SARs illuminate a region on the surface as shown in Fig. 2. The first pair of instruments illuminate the surface with look angles $\theta_{1_T}, \theta_{1_R}$ and squints ψ_{1_T}, ψ_{1_R}, while the second pair has look angles $\theta_{2_T}, \theta_{2_R}$ and squints ψ_{2_T}, ψ_{2_R}, where subscripts T and R refer to the transmitter and the receiver, respectively. The azimuth direction is x and the ground range direction is y; the two-way slant range to the center of the resolution cell is R_0. The signal representing the processed image of the ith SAR for $i \in \{1, 2\}$ is

$$u_i(x, y) = e^{-jk_0R_0}(f_i * \chi)(x, y) \tag{6}$$

where $\chi(x, y)$ denotes the system impulse response in terms of azimuth and ground range. We introduce the following symbols in the interest of brevity:

$$f_i(x, y) = s(x, y)e^{-j\boldsymbol{k_i}\cdot\boldsymbol{r_s}} \tag{7}$$

$$\boldsymbol{r_s} = (x, y, z(x, y))^T \tag{8}$$

$$\boldsymbol{k_{i_T}} = k_0(\sin\psi_{i_T}, \cos\psi_{i_T}\sin\theta_{i_T}, -\cos\psi_{i_T}\cos\theta_{i_T})^T \tag{9}$$

$$\boldsymbol{k_{i_R}} = k_0(\sin\psi_{i_R}, \cos\psi_{i_R}\sin\theta_{i_R}, -\cos\psi_{i_R}\cos\theta_{i_R})^T \tag{10}$$

$$\boldsymbol{k_i} = \boldsymbol{k_{i_T}} + \boldsymbol{k_{i_R}} \tag{11}$$

where $\boldsymbol{k_i}$ is the ith bistatic wave vector, and we have assumed that the surface scattering described by the reflectivity $s(x, y)$ is coming from the surface described by $z(x, y)$. The carrier wavenumber, $k_0 = 2\pi/\lambda_0$, depends on the carrier wavelength λ_0 of the instrument, which we assume is common between the two sensors. The wave vectors $\boldsymbol{k_{i_T}}$ and $\boldsymbol{k_{i_R}}$ are equivalent to those in Section II-A, but here we have defined them in terms of the look and squint angles of the instruments instead of the gradients of the slant ranges. In monostatic operation, the wave vector $\boldsymbol{k_i}$ reduces to $2\boldsymbol{k_{i_T}}$, and the modulus is two times the carrier wavenumber. The modulus of the bistatic wave vector is smaller than $2k_0$.

We express a single realization of an interferogram as

$$V(x, y) = u_1(x, y)u_2(x, y)^*. \tag{12}$$

The Fourier transform of the interferogram is

$$\begin{aligned}\tilde{V}(k_x', k_y') &= \mathcal{F}\{u_1(x, y)u_2(x, y)^*\}(k_x, k_y)\\ &= (\tilde{u}_1 \star \tilde{u}_2)(k_x, k_y)\\ &= \int\int \tilde{u}_1(k_x, k_y)^*\tilde{u}_2(k_x + k_x', k_y + k_y')\,\mathrm{d}k_x\,\mathrm{d}k_y\end{aligned} \tag{13}$$

where $\star$ denotes the cross correlation operation and the Fourier transform of the image (6) is given by

$$\tilde{u}_i(k_x, k_y) = \tilde{f}_i(k_x, k_y)\tilde{\chi}(k_x, k_y). \tag{14}$$

Assuming that the vertical component of $\boldsymbol{r_s}$ is constant with x and y allow us to express the Fourier transform of the image as the shifted reflectivity filtered by the instrument frequency response in the wavenumber domain

$$\tilde{u}_i(k_x, k_y) = \tilde{s}(k_x + \boldsymbol{k_{i_x}}, k_y + \boldsymbol{k_{i_y}})e^{-j\boldsymbol{k_{i_z}}z}\tilde{\chi}(k_x, k_y) \tag{15}$$

where the notation $\boldsymbol{k_{i_j}}$ denotes the jth component of wave vector $\boldsymbol{k_i}$ and $j \in \{x, y, z\}$. Equation (15) states that each sensor samples the surface reflectivity across a band of range and azimuth wavenumbers. Since the surface reflectivity is not bandlimited, the bandwidth of the image is determined by the system frequency response. Each ground-range and azimuth wavenumber at which the sensor samples the reflectivity is shifted by $\boldsymbol{k_{i_y}}$ and $\boldsymbol{k_{i_x}}$, respectively. Thus, each instrument captures a different wavenumber band of the surface reflectivity. The band that each instrument captures depends on the wave vector of the instrument.

Substituting (15) into (13) yields the linear cross correlation of the two image spectra

$$\begin{aligned}\tilde{V}(k_x, k_y) = \int\int &\tilde{s}(k_x' + \boldsymbol{k_{1_x}}, k_y' + \boldsymbol{k_{1_y}})^*\\ &\cdot \tilde{s}(k_x' + \boldsymbol{k_{2_x}} + k_x, k_y' + \boldsymbol{k_{2_y}} + k_y)\end{aligned}$$

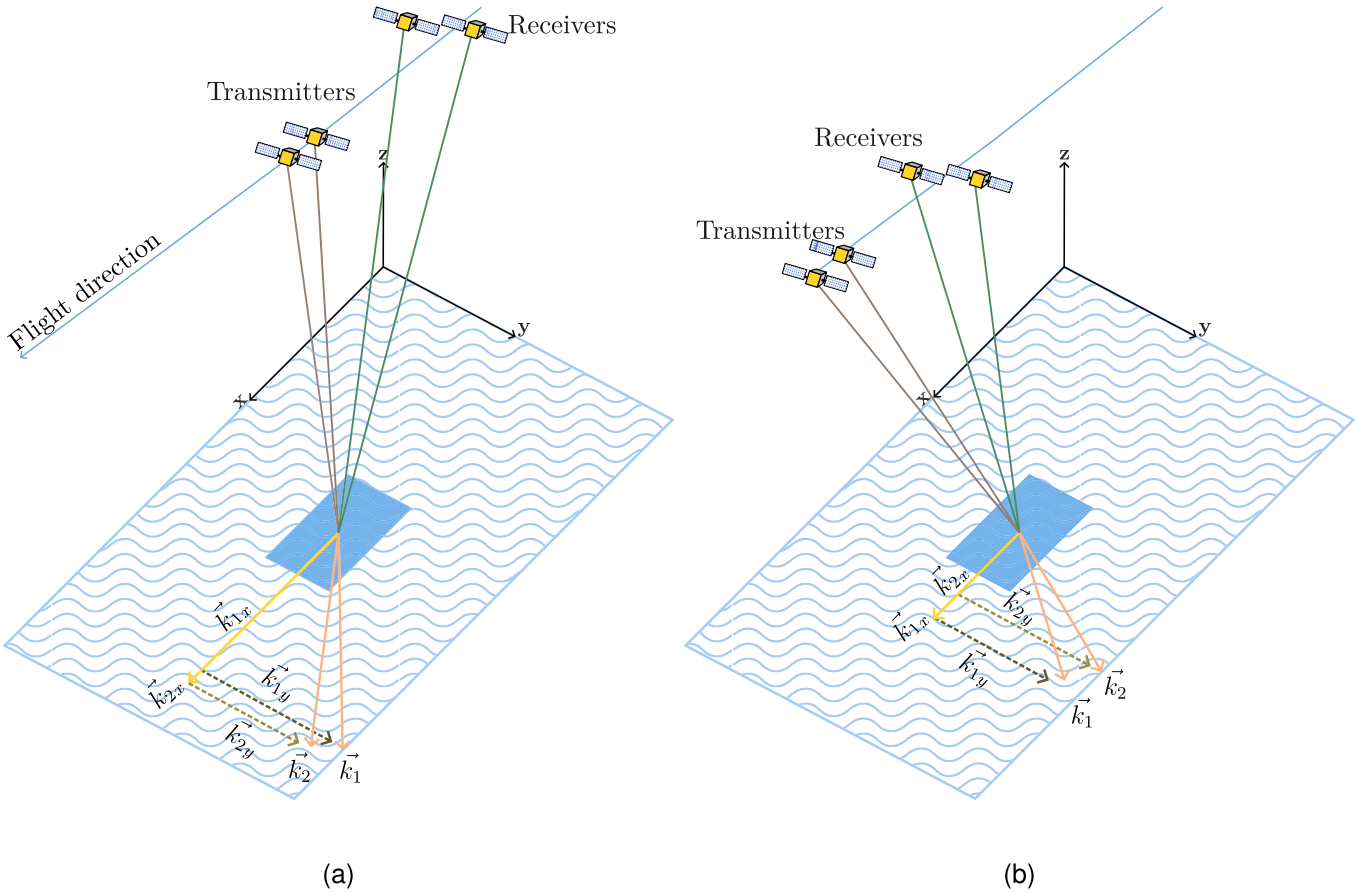

Fig. 2. Illustration of the two SAR instruments sampling ground-projected range and azimuth wavenumbers of a given resolution cell. $\boldsymbol{k_i}$ is the surface-projected wavenumber vector that the ith instrument samples. (a) Beginning of an acquisition. (b) End of an acquisition.

$$\cdot\, e^{j\Delta \boldsymbol{k}_z z}\tilde{\chi}\left(k_x', k_y'\right)^* \cdot \tilde{\chi}\left(k_x' + k_x, k_y' + k_y\right) \mathrm{d}k_x' \,\mathrm{d}k_y' \tag{16}$$

where $\Delta \boldsymbol{k}_z = \boldsymbol{k_{1}}_z - \boldsymbol{k_{2}}_z$ is the z component of the wave vector difference.

We assume that the surface reflectivity, $s(x, y)$, is a circular complex stochastic process. Thus, as shown in the Appendix, the Fourier transform of the surface reflectivity, $\tilde{s}(k_x, k_y)$, is uncorrelated

$$\mathbb{E}\{\tilde{s}(k_x, k_y)\tilde{s}(\kappa_x, \kappa_y)^*\} = \tilde{R}_s(k_x, k_y)\delta(k_x - \kappa_x, k_y - \kappa_y) \tag{17}$$

where $\tilde{R}_s(k_x, k_y)$ is the Fourier transform of the surface reflectivity's spatial correlation. For a wide-sense stationary process $\tilde{R}_s(k_x, k_y)$ is the power spectral density of the surface reflectivity, according to the Wiener–Khinchin theorem. The Dirac delta function in (17) represents an idealized case, which follows from the assumption that at the scales of interest, the autocorrelation length of the surface roughness is short. A practical surface can be modeled by replacing the Dirac delta with a finite-bandwidth function, such as a Gaussian kernel, to model the distribution of the power spectral density over a band of wavenumbers.

We are interested in the expected interferogram, so we take the expectation over the surface ensemble of (16) and apply (17)

$$\tilde{I}(k_x, k_y) = \int\int \tilde{R}_s\left(k_x' + \boldsymbol{k_{1}}_x, k_y' + \boldsymbol{k_{1}}_y\right) \cdot \delta(k_x + \Delta \boldsymbol{k}_x, k_y + \Delta \boldsymbol{k}_y) \cdot e^{j\Delta \boldsymbol{k}_z z}\tilde{\chi}\left(k_x', {k_y}'\right)^* \cdot \tilde{\chi}\left(k_x' + k_x, k_y' + k_y\right) \mathrm{d}k_x' \,\mathrm{d}k_y' \tag{18}$$

where $\Delta \boldsymbol{k}_x = \boldsymbol{k_{1}}_x - \boldsymbol{k_{2}}_x$, and $\Delta \boldsymbol{k}_y = \boldsymbol{k_{1}}_y - \boldsymbol{k_{2}}_y$. The Dirac delta function is not a function of the integration variables, so we can move it out of the integral. We describe $\tilde{I}$ as the product of the delta function and the cross correlation of the frequency response with itself filtered by the power spectral density of the surface reflectivity

$$\tilde{I}(k_x, k_y) = \delta(k_x + \Delta \boldsymbol{k}_x, k_y + \Delta \boldsymbol{k}_y)e^{j\Delta \boldsymbol{k}_z z} \times \left(\tilde{R}_s' X \star X\right)(k_x, k_y) \tag{19}$$

where $\tilde{R}_s'$ is the shifted Fourier transform of the spatial correlation of the surface reflectivity $\tilde{R}_s'(k_x, k_y) = \tilde{R}_s(k_x + \boldsymbol{k_{1}}_x, k_y + \boldsymbol{k_{1}}_y)$. Taking the inverse Fourier transform of (19) yields

$$\begin{aligned} I(x, y) &= \mathcal{F}^{-1}\{\tilde{I}(k_x, k_y)\}(x, y) \\ &= e^{j\Delta \boldsymbol{k}_z z}\tilde{K}(\Delta \boldsymbol{k}_x, \Delta \boldsymbol{k}_y)e^{j(\Delta \boldsymbol{k}_x x + \Delta \boldsymbol{k}_y y)} \end{aligned} \tag{20}$$

where $\tilde{K}(k_x, k_y) = (\tilde{R}_s'\tilde{\chi} \star \tilde{\chi})(k_x, k_y)$. We can readily interpret (20). The expected interferogram is a complex sinusoid in the spatial domain, with phase proportional to the height of the surface. The amplitude is the wavenumber-domain cross correlation of the product $\tilde{R}_s'\tilde{\chi}$ with the system frequency response, evaluated at the shift between the two images. The product $\tilde{R}_s'\tilde{\chi}$ is the frequency response of the system filtered by the shifted power spectral density of the reflectivity.

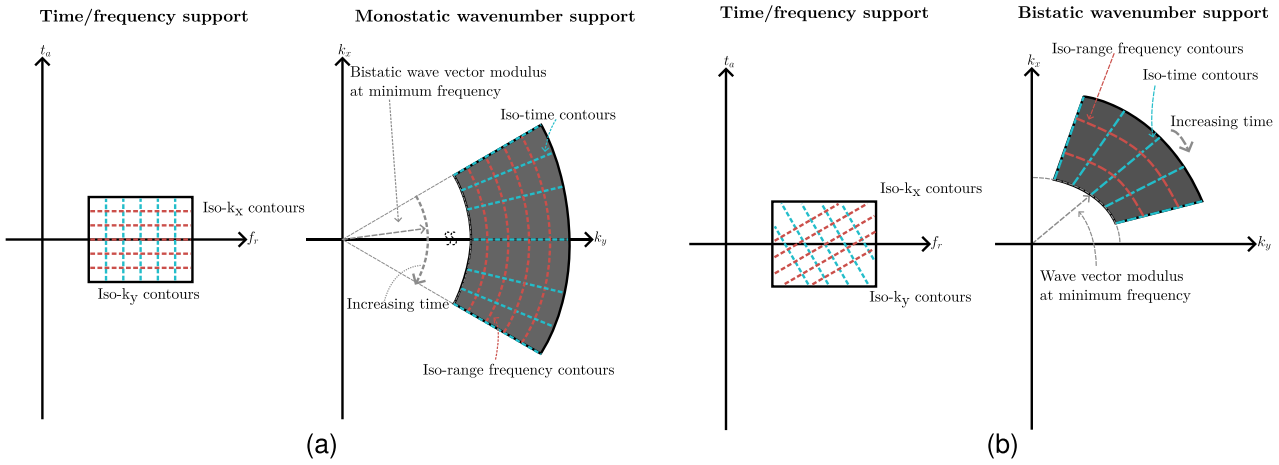

Fig. 3. Time–frequency and the corresponding wavenumber region of support of a resolution cell for (a) monostatic and (b) bistatic interferometers. We note that the modulus of the bistatic wave vectors is smaller than that of the monostatic wave vectors for the same range frequency. We illustrate the modulus of the bistatic wave vector at the minimum range frequency in both support diagrams. The difference in the moduli is exaggerated in the diagram for illustration. Furthermore, the aperture time that we consider for these diagrams is larger than what is typically used in real-world systems to illustrate the shape of the region of support. In a real-world radar, the wavenumber region of support in (a) would look rectangular, and that in (b) trapezoidal, as they would only be a slice of illustrated regions.

C. Wavenumber Support

We express the wavenumber support of a SAR image as a function of slow time, t, and range frequency f_r. The wavenumbers forming the support of a resolution cell located at the transmitter look angle θ_l satisfy

$$\boldsymbol{k_i}(t,\, f_r;\, \theta_l) = k_0(f_r)(\hat{\boldsymbol{l}}_{\boldsymbol{T_i}}(t) + \hat{\boldsymbol{l}}_{\boldsymbol{R_i}}(t)) \tag{21}$$

where $k_0(f_r) = 2\pi f_r/c_0$ is the wavenumber magnitude, $\hat{\boldsymbol{l}}_{\boldsymbol{T_i}}$ is the unit vector in the direction of the transmitter's line of sight, and $\hat{\boldsymbol{l}}_{\boldsymbol{R_i}}$ is the unit vector in the direction of the receiver's line of sight. The line of sight of the ith sensor is

$$\hat{\boldsymbol{l}}_{\boldsymbol{S_i}}(t) = \frac{\boldsymbol{r}_{\boldsymbol{S_i}}(t) - \boldsymbol{r_p}}{\|\boldsymbol{r}_{\boldsymbol{S_i}}(t) - \boldsymbol{r_p}\|} \tag{22}$$

where S is either T for the transmitter line of sight, or R for the receiver line of sight, and $\boldsymbol{r_p}$ is the position vector of the resolution cell. The time variable for a given resolution cell varies from $\tau_c - \tau_l/2$ to $\tau_c + \tau_l/2$, where τ_c is the beam center time and τ_l is the illumination duration. The range frequency is centered around the carrier frequency, f_c, and its bounds are given by the bandwidth of the transmitted pulse.

Equation (21) provides insights into the relationship between the signal space and the observation space. For a given resolution cell, slow time and range frequency parameterize the signal space, while in the observation space range and azimuth wavenumbers are the parameters. Assume the conventional viewing geometry of a monostatic SAR that is looking perpendicular to the azimuth direction. For a given slow time, the instrument samples the resolution cell with a band of frequencies determined by the transmitted pulse. The sampling of the resolution cell repeats every pulse repetition interval during the illumination time. The locus of slow time and range frequency that make up the samples of the resolution cell are shown on the left panel of Fig. 3(a). The vertical extent of the region is the illumination time of the instrument, and the width is the pulse bandwidth.

The support of the signal in terms of slow time and range frequency maps to wavenumbers projected on the plane tangent to the surface at the resolution cell according to (21). The region of support of a resolution cell in terms of wavenumbers is shown in the right panel of Fig. 3(a). The diagram has been produced by exaggerating the illumination time to highlight the curvature of the region of support as time moves away from the beam center time.

We now move on to a bistatic case with a common transmitter. Assume that the transmitter maintains the same viewing geometry and transmits the same pulse as in the previous case. The receiver lags the transmitter along the same orbital plane. As a result, $\hat{\boldsymbol{l}}_{\boldsymbol{R}}$ is squinted forward with respect to $\hat{\boldsymbol{l}}_{\boldsymbol{T}}$. Since the transmitted pulse and the illumination time have not changed, the time-frequency support of the signal is the same as before. However, the different viewing geometry changes the mapping to the wavenumber domain. The squint of the bistatic line of sight means that for a fixed slow time, as the range frequency is sweeping, both the range and the azimuth wavenumbers are changing, as Fig. 3(b) shows. Additionally, for a fixed range frequency the line of sight of the instrument is always squinted, which breaks the symmetry of the wavenumber support about k_x. The coupling of the range and azimuth wavenumbers means that there are no longer separable in terms of time and range frequency. The isolines in the left panel of Fig. 3(b) show that a fixed value of range or azimuth wavenumbers traverses both time and frequency.

D. Temporal Lag and Spectral Shift

We are interested in the difference between the supports of two SAR images acquired by two instruments with a physical separation $\Delta\boldsymbol{r}(t)$. We express the wavenumbers in the support of the first sensor by setting $i = 1$ in (21), and define the support of the second sensor as

$$\boldsymbol{k_2}(t,\, f_r;\, \theta_l) = k_0(f_r)\big(\hat{\boldsymbol{l}}_{\boldsymbol{T_1}}(t) + \hat{\boldsymbol{l}}_{\boldsymbol{R_1}}(t) + \Delta\boldsymbol{l_T}(t) + \Delta\boldsymbol{l_R}(t)\big) \tag{23}$$

where

$$\Delta\boldsymbol{l_S}(t) = \frac{\boldsymbol{r}_{\boldsymbol{S_1}}(t) + \Delta\boldsymbol{r_S}(t) - \boldsymbol{r_p}}{\|\boldsymbol{r}_{\boldsymbol{S_1}}(t) + \Delta\boldsymbol{r_S}(t) - \boldsymbol{r_p}\|} - \hat{\boldsymbol{l}}_{\boldsymbol{S_1}}(t) \tag{24}$$

is the difference between the line of sight vectors due to the relative position of the second instrument with respect to the first. The first-order Taylor expansion of (23) about (τ_c, f_c) is

$$\begin{aligned}\boldsymbol{k_2}(t, f_r; \theta_l) \approx (k_0 + \Delta k)(\hat{\boldsymbol{l}}_{\boldsymbol{T_1}}(\tau_c) + \hat{\boldsymbol{l}}_{\boldsymbol{R_1}}(\tau_c) + \Delta \boldsymbol{l_T}(\tau_c) \\ + \Delta \boldsymbol{l_R}(\tau_c)) + k_0 \frac{\partial}{\partial t}(\hat{\boldsymbol{l}}_{\boldsymbol{T_1}} + \hat{\boldsymbol{l}}_{\boldsymbol{R_1}} \\ + \Delta \boldsymbol{l_T} + \Delta \boldsymbol{l_R})(\tau_c)\Delta t \qquad (25) \\ = \boldsymbol{k_1}(t, f_r; \theta_l) + (k_0 + \Delta k)\Delta \boldsymbol{l}(\tau_c) \\ + k_0 \frac{\partial \Delta \boldsymbol{l}}{\partial t}(\tau_c)\Delta t \qquad (26)\end{aligned}$$

where we have used $k_0 = k_0(f_c)$, $\Delta k = (\partial k_0/\partial f_r)(f_c)(f_r - f_c)$, $\Delta t = t - \tau_c$, $\Delta \boldsymbol{l} = \Delta \boldsymbol{l_T}(\tau_c) + \Delta \boldsymbol{l_R}(\tau_c)$ for brevity, and we have neglected $\Delta f \Delta t$ cross terms.

To align the two images we fix the support of the first image at the beam crossing time and at the center frequency and solve for the $(\Delta t, \Delta k)$ where the second support intersects the first

$$\boldsymbol{k_1}(\tau_c, f_c; \theta_l) = \boldsymbol{k_2}(t, f_r; \theta_l). \qquad (27)$$

Simplifying (27) leads to

$$\Delta k(\boldsymbol{l} + \Delta \boldsymbol{l}) + k_0 \frac{\partial(\boldsymbol{l} + \Delta \boldsymbol{l})}{\partial t}(\tau_c)\Delta t = -k_0 \Delta \boldsymbol{l}(\tau_c) \qquad (28)$$

where $\boldsymbol{l} = \hat{\boldsymbol{l}}_{\boldsymbol{T_1}}(\tau_c) + \hat{\boldsymbol{l}}_{\boldsymbol{R_1}}(\tau_c)$.

Until now, no assumption has been made on the reference frame of vectors $\boldsymbol{k_1}$ and $\boldsymbol{k_2}$. Recalling Section II-B, the information in the interferogram comes from the surface-projected wavenumbers where the regions of support of the two images coincide. Thus, to relate the difference in the support to the temporal lag and spectral shift, we need to solve (27) in a reference frame where two of the basis vectors are aligned with the ground range and azimuth directions. Equation (28) is an overdetermined system of three equations and two unknowns. However, we can remove one equation from the system by projecting the wavenumbers on the plane tangent to the surface. After coordinate transformation and projection, (27) becomes

$$\boldsymbol{k_{1xy}}(\tau_c, f_c; \theta_l) = \boldsymbol{k_{2xy}}(t, f_r; \theta_l) \qquad (29)$$

where $\boldsymbol{k_{1xy}}(\tau_c, f_c; \theta_l) = \boldsymbol{\Gamma k_1}(\tau_c, f_c; \theta_l)$ and $\boldsymbol{k_{2xy}}(t, f_r; \theta_l) = \boldsymbol{\Gamma k_2}(t, f_r; \theta_l)$ and $\boldsymbol{\Gamma}$ is a matrix representing the surface projection to the tangent plane of the resolution cell. Fig. 4 shows the tangent plane for a given point on the surface, the two basis vectors along the plane and the basis vector normal to the plane, and the wave vectors of two instruments and their projections at the temporal lag and spectral shift where they align.

We model the surface projection by

$$\boldsymbol{\Gamma} = \boldsymbol{Q_{Xx}}\left(\boldsymbol{I} - \hat{\boldsymbol{n}}\hat{\boldsymbol{n}}^T\right) \qquad (30)$$

where $\boldsymbol{Q_{Xx}}$ is the direction cosine matrix from the reference frame that the vectors are expressed into the local tangent frame, and $\hat{\boldsymbol{n}}$ is the unit vector normal to the surface expressed in the reference frame of the wavenumber vectors. We define the local tangent plane with two basis vectors that lie within the the plane, one aligned with the interferogram's ground range direction and one with the azimuth direction, and complete it with $\hat{\boldsymbol{n}}$. The second term of (30) projects the vector on the tangent plane, while the first term transforms the vector to the local tangent frame. Hence, a vector multiplied by $\boldsymbol{\Gamma}$ defined in (30) will have a third component equal to zero.

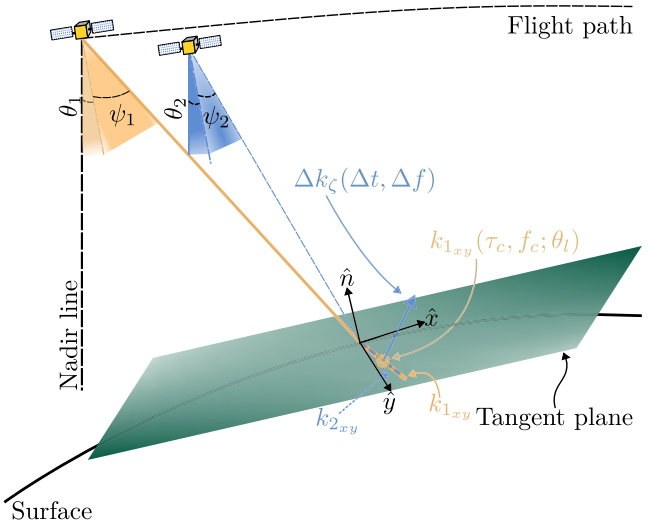

Fig. 4. Plane tangent to a given point on the surface and the basis vectors of the reference frame used to align the wavenumber support of the two SAR systems. Two SAR satellites with different look angles and squints are shown. The wave vectors of the first and second systems are shown in orange and blue colors, respectively. For ease of illustration, the figure omits the transmitting satellites and instead displays two monostatic satellites; thus the bistatic wave vector reduces to $\boldsymbol{k_i} = 2\boldsymbol{k_{i_T}}$. The concept remains the same for bistatic systems. The surface-projected wave vectors of the two instruments, $\boldsymbol{k_{1_{xy}}}$ and $\boldsymbol{k_{2_{xy}}}$, at the moment of alignment, are shown on the tangent plane. The circle at the midpoint of $\boldsymbol{k_{1_{xy}}}$ represents the point at which we fix the support of the first acquisition when solving (29). The figure also illustrates the component of the difference of the aligned wave vectors in the elevation direction, $\Delta \boldsymbol{k}_\zeta(\Delta t, \Delta f)$. The difference of these vectors drives the sensitivity to the surface height.

Multiplying both sides of (28) by $\boldsymbol{\Gamma}$ yields

$$\begin{pmatrix} k_0\left(\frac{\partial(\boldsymbol{l} + \Delta \boldsymbol{l})}{\partial t}(\tau_c)\right)_x & (\boldsymbol{l} + \Delta \boldsymbol{l})_x \\ k_0\left(\frac{\partial(\boldsymbol{l} + \Delta \boldsymbol{l})}{\partial t}(\tau_c)\right)_y & (\boldsymbol{l} + \Delta \boldsymbol{l})_y \end{pmatrix} \begin{pmatrix} \Delta t \\ \Delta k \end{pmatrix} = -k_0 \Delta \boldsymbol{l}. \qquad (31)$$

Equation (31) provides an analytic solution to Δt and Δk, and it is valid if Δt and Δk are sufficiently small for second- and higher-order terms to be neglected. In cases where the first-order expansion is invalid, we can compute the solution to (27) numerically using an optimization method.

E. Height Sensitivity

After solving for the temporal and spectral shift according to (31), the sensitivity can be computed from the difference of the aligned wavenumber supports. The interferometric phase of a resolution cell is

$$\phi(\Delta t, \Delta f) = \Delta \boldsymbol{k}(\Delta t, \Delta f) \cdot \boldsymbol{\zeta} \qquad (32)$$

where $\boldsymbol{\zeta}$ is the elevation vector and $\Delta \boldsymbol{k}(\Delta t, \Delta f)$ is the difference of the aligned supports

$$\Delta \boldsymbol{k}(\Delta t, \Delta f) = \boldsymbol{k_2}(\tau + \Delta t, f_c + \Delta f; \theta_l) - \boldsymbol{k_1}(\tau, f_c; \theta_l). \qquad (33)$$

Fig. 4 illustrates the supports of the aligned surface-projected wavenumber supports. The orange line on the tangent plane represents the surface projection of the first support $\boldsymbol{k_{1_{xy}}}$ at the

beam crossing time τ_c. Examining the definition of the wave vector in (21) reveals that by not fixing the range frequency of the wave vector, $\boldsymbol{k}_{\mathbf{1}_{xy}}$ becomes a line that is parallel to the surface projection of the line of sight and passes through the origin. At the solution of (29), the surface-projected support of the second wave vector coincides in the Fourier space with the surface-projected support of the first acquisition at the beam crossing time and center frequency. While the surface projections of the supports are equal to each other, their components in the normal direction to the surface are different. The dot product of this difference with the elevation gives rise to the interferometric phase and drives the sensitivity.

In a SAR image, a scatterer is placed at the intersection of the iso-range and iso-Doppler surfaces. In the monostatic case, these reduce to the known iso-range sphere and iso-Doppler cone. Generally, the range and Doppler surfaces are

$$R \text{ ellipsoid: } R = \|\boldsymbol{l}_T(t)\| + \|\boldsymbol{l}_R(t)\| \tag{34}$$

$$\begin{aligned} f_D \text{ surface: } f_D &= \frac{1}{\lambda_c}\left(\hat{\boldsymbol{l}}_T(t)\cdot\boldsymbol{v}_T(t) + \hat{\boldsymbol{l}}_R(t)\cdot\boldsymbol{v}_R(t)\right) \\ &= \tilde{\nu}_c\Big(\hat{\boldsymbol{l}}_{T0}(t)\cdot\boldsymbol{v}_T(t) + \hat{\boldsymbol{l}}_{R0}(t)\cdot\boldsymbol{v}_R(t) \\ &\quad + \frac{\boldsymbol{r}}{\|\boldsymbol{l}_{T0}(t)+\boldsymbol{r}\|}\cdot\boldsymbol{v}_t(t) \\ &\quad + \frac{\boldsymbol{r}}{\|\boldsymbol{l}_{R0}(t)+\boldsymbol{r}\|}\cdot\boldsymbol{v}_R(t)\Big) \\ &\approx f_D(\boldsymbol{r_0}) + \tilde{\nu}_c\boldsymbol{r}\cdot\left(\frac{\boldsymbol{v}_T(t)}{\|\boldsymbol{l}_{T0}\|} + \frac{\boldsymbol{v}_R(t)}{\|\boldsymbol{l}_{R0}\|}\right) \end{aligned} \tag{35}$$

where in the equation of the Doppler shift we have expressed the scatterer location as the sum of a reference position and a relative position $\boldsymbol{r}_p = \boldsymbol{r_0} + \boldsymbol{r}$ and approximated $\|\boldsymbol{l}_{T0}(t) + \boldsymbol{r}\|$ and $\|\boldsymbol{l}_{R0}(t) + \boldsymbol{r}\|$ as $\|\boldsymbol{l}_{T0}\|$ and $\|\boldsymbol{l}_{R0}\|$ respectively. The locus of points that satisfy conditions (34) and (35) is a line. Conventionally, SAR images are focused at the zero-Doppler location, that is, $f_D = 0$. Thus, the solution lies on a line on the surface of the range ellipsoid. All scatterers at the same range and with the same zero-Doppler location are positioned along this line, regardless of the incidence angle of their location.

Cross-track interferometry (XTI) solves for the missing third dimension by positioning a scatterer at a look angle on the line of constant range and Doppler. After applying the plane-wave approximation at the vicinity of the scatterer, the curve along which the solution lies becomes a straight line. XTI locates the scatterer along the fronts of the plane wave. Hence, an interferometer is sensitive to the elevation along this line, normal to the range and Doppler directions. The height normal to the surface is related to the elevation

$$z(t) = \zeta(t)\hat{\boldsymbol{\xi}}\cdot\hat{\boldsymbol{z}} \tag{36}$$

where $\boldsymbol{\zeta}$ is orthogonal to both the iso-range lines and the iso-Doppler lines

$$\boldsymbol{\zeta} = (\hat{\boldsymbol{l}}_T + \hat{\boldsymbol{l}}_R)\times\left(\frac{\boldsymbol{v}_T}{\|\boldsymbol{l}_T\|} + \frac{\boldsymbol{v}_R}{\|\boldsymbol{l}_R\|}\right) \tag{37}$$

and $\hat{\boldsymbol{\xi}} = \boldsymbol{\zeta}/\|\boldsymbol{\zeta}\|$.

Taking the derivative of the interferometric phase (32) with respect to height yields the sensitivity of the interferometer to height

$$\frac{\partial\phi}{\partial z} = \Delta\boldsymbol{k}_\zeta(\Delta t, \Delta f)\frac{\partial\zeta}{\partial z} \tag{38}$$

where $\Delta\boldsymbol{k}_\zeta(\Delta t, \Delta f)$ is the ζ component of the aligned support difference and from (36), we can express the derivative of the elevation with respect to height as $1/\hat{\boldsymbol{\xi}}\cdot\hat{\boldsymbol{z}}$. Thus, the sensitivity is the difference between the aligned supports, in the elevation direction, inverted to the vertical direction.

TABLE I
PARAMETERS OF THE INTERFEROMETER USED IN DIFFERENT SIMULATION SCENARIOS

Case	$a\Delta e$ / m	$a\Delta\Omega$ / m	Operation
1	50	0	Monostatic & Bistatic
2	0	650	Bistatic
3	125	650	Bistatic

III. SIMULATIONS AND RESULTS

A. Simulations

We simulate three different interferometers. In all three, the receiving SAR satellites are flying in a Helix formation [17]. The first has a tangential and radial separation between the two sensors, and we simulate both monostatic and bistatic operations with a common transmitter. The two antennas point in the zero-Doppler direction. The second also looks in the zero-Doppler direction, but only has a normal separation and operates monostatically. Thus, the effective temporal lag is 0 s. The third is a system inspired by Harmony and consists of three SAR satellites: an illuminator and two formation-flying receivers, that lag the illuminator by 350 km [18]. The Helix formation combines radial, normal, and tangential separations that vary sinusoidally along the orbit. Due to the bistatic operation, the two receivers are looking forward, that is, they have a squint, with respect to the zero-Doppler direction. Table I lists the parameters of the three simulation scenarios, where $a\Delta e$ and $a\Delta\Omega$ are the magnitudes of the relative eccentricity and relative inclination vectors of the formation, as defined in [17], and both vectors have a phase of $-\pi/2$. Fig. 5 illustrates the satellite configurations of the three cases.

The first two scenarios use a formation that models a pure ATI and a pure XTI, respectively. In the first case, we expect the temporal lag calculated using the wavenumber method to match the along-track physical separation between the two formation satellites. Similarly, we expect the sensitivity of the XTI to match the sensitivity calculated from the conventional equation in the second case. We simulate the second case in a flat-Earth frame to eliminate the effect of the Earth's rotation and curvature. In the other cases, we carry out the simulations in an Earth-centered The earth-fixed frame before transforming to a local-tangent local-normal frame as discussed in (30).

The last scenario poses challenges, as it cannot be accurately modeled with conventional geometric approaches. The combination of bistatic operation and a squinted line of sight results in under or overestimating the temporal lag if only the physical separation is used. Locating the shift needed for the lines of sight of the two receivers to align yields a more accurate estimate, but the bistatic operation means that the two

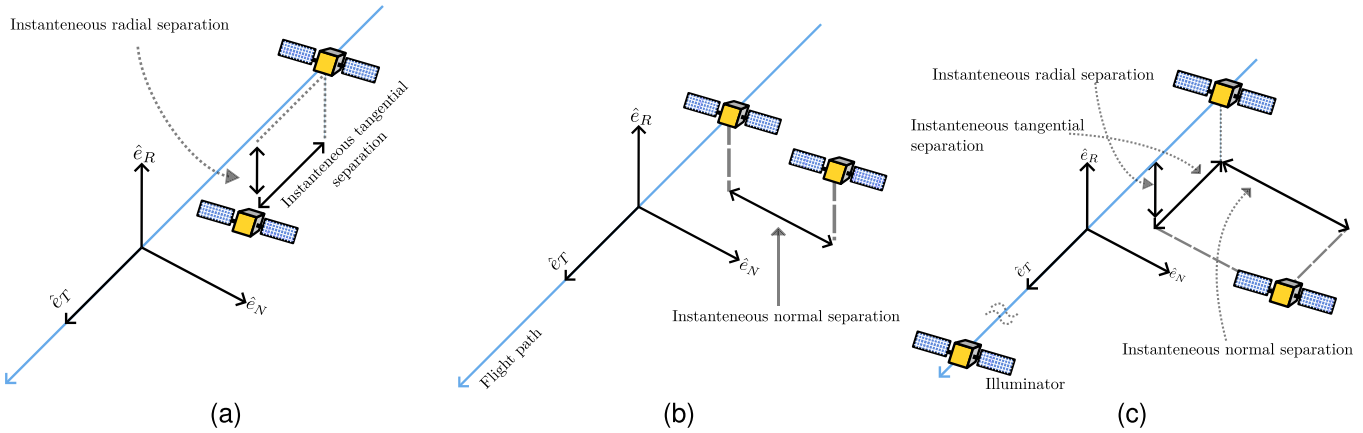

Fig. 5. Illustration of the three different satellite configurations used for the simulation experiments. (a) First case, with a tangential and radial component that varies with time. (b) Second case, with only a normal component that varies with time. (c) Third case, with separations in all three directions varying with time.

receivers do not have a single line of sight between them and the surface.

Using the ME can offer a way out, but the questions of where to place the equivalent system and how to convert the along-track and perpendicular baselines of the formation to those of the equivalent system is not trivial. Our numerical experiments have shown that using the geometric method of aligning the monostatically equivalent lines of sight of the two systems approach the results of the wavenumber method when the ME system is placed at the intersection of the bistatic line of sight and the line segment between the transmitter and the receiver. Hence, a unique ME exists for each combination of incidence angle and slow time, as Fig. 1 illustrates. The geometric method is explained in detail in the appendix.

B. Results

In this section, we present the temporal lag and sensitivity to height of three different interferometric configurations based on computational simulations. Fig. 6 shows the temporal lag of a Helix interferometer with only an $a\Delta e$ component (case 1). This means that the along-track separation of the interferometer varies sinusoidally along the orbit with an amplitude of $2a\Delta e$ [17]. The temporal lag of a monostatic interferometer that looks perpendicular to the flight direction is equal to the along-track separation divided by the flight velocity. If the interferometer operates bistatically, then the along-track baseline halves. The along-track baseline, calculated using the wavenumber method of (31), matches the expected result.

Fig. 7 illustrates the sensitivity to height of a Helix formation that has a separation only in the normal direction (case 2). The sensitivity is calculated as follows.

1) Find the temporal lag and a frequency shift given by (31).
2) Compute the spectral support of the first sensor at the beam crossing time and the center frequency. Compute the spectral support of the second sensor at the shifts found in the previous step.
3) Calculate the sensitivity using (38).

The sensitivity of a monostatic XTI with an unsquinted line of sight is described by the well-known expression in the literature [4], [5]. The right panel in Fig. 7 shows the relative error between the sensitivity calculated using the method

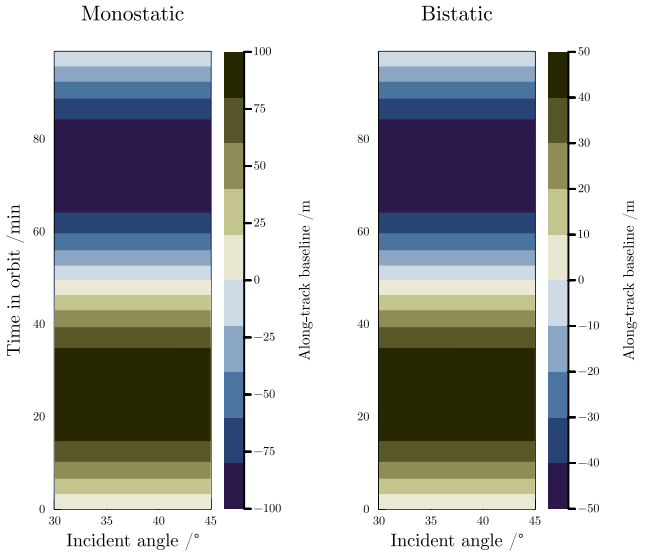

Fig. 6. Temporal lag of case number 1 in Table I. The left panel shows the temporal lag of a monostatic interferometer and the right panel that of a bistatic interferometer.

proposed in this article and the classical expression of the interferometric sensitivity.

Moving on to a more complex geometry, Fig. 8 shows the temporal lag of Helix interferometer with $a\Delta e = 125$ m and $a\Delta\Omega = 650$ m (case 3). In this case, two factors complicate the geometry.

1) The bistatic operation of the receivers with an illuminator that is significantly ahead of the Helix formation.
2) The significant line-of-sight squint of the receiving instruments that is needed to follow the transmitter's beam.

We compare the temporal lag obtained using the wavenumber method to the temporal lag calculated using the geometric method of finding the along-track shift that aligns the lines of sight of the monostatic equivalents. The absolute error between the two methods peaks at 0.40 ms.

The sensitivity to height of the configuration is shown in the left panel of Fig. 9. The right panel displays the relative difference between the spectrally derived sensitivity and the sensitivity calculated using the ME method explained

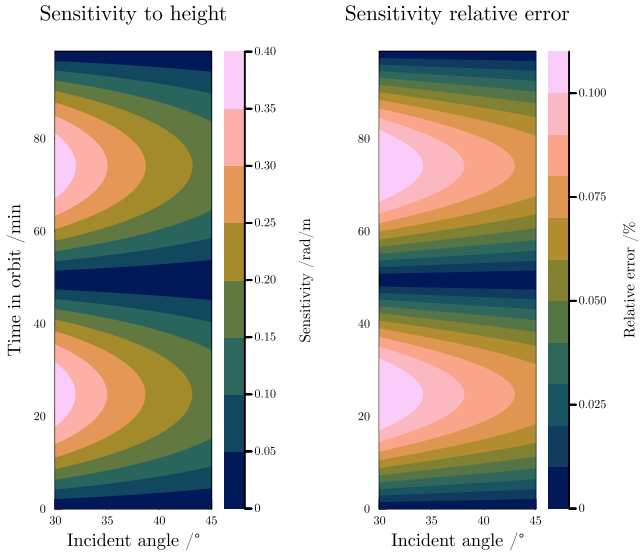

Fig. 7. Formation with a 650 m ascending node difference. Left panel: The sensitivity to height. Right panel: The relative error of the sensitivity calculated using the wavenumber method with respect to the conventional sensitivity expression.

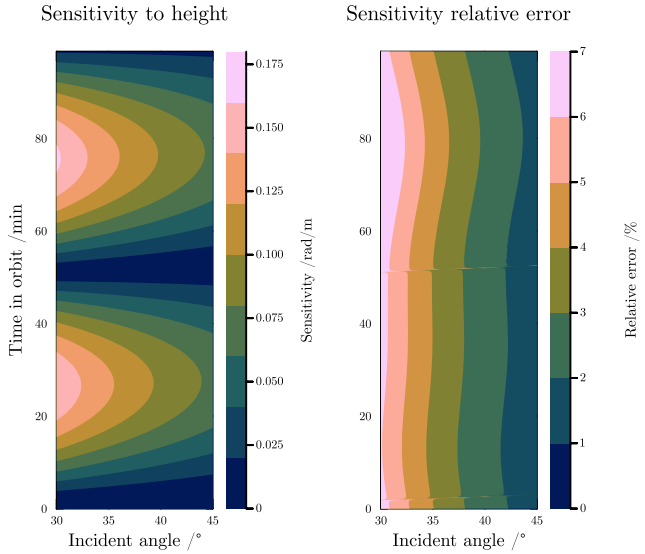

Fig. 9. Formation with a 650 m ascending node difference and a 125 m radial difference. Left panel: The sensitivity to height. Right panel: The relative error of the sensitivity calculated using the wavenumber method with respect to the conventional sensitivity expression.

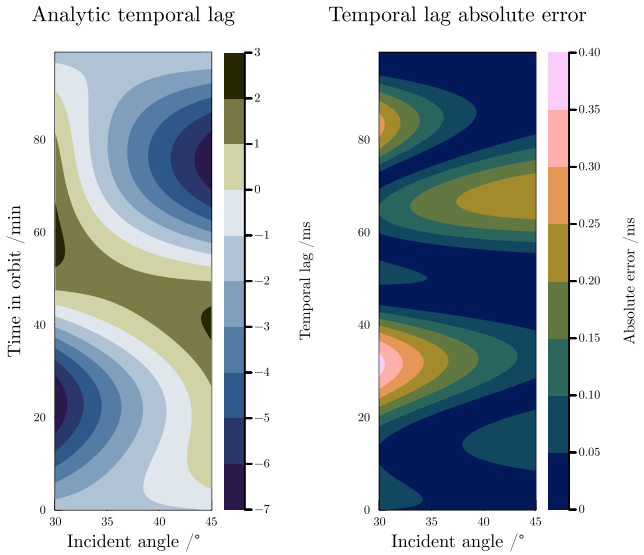

Fig. 8. Formation with a 650 m ascending node difference and a 125 m radial difference. Left panel: The temporal lag using the wavenumber method. Right panel: The absolute error between the temporal lag calculated spectrally and the temporal lag calculated using the geometric method.

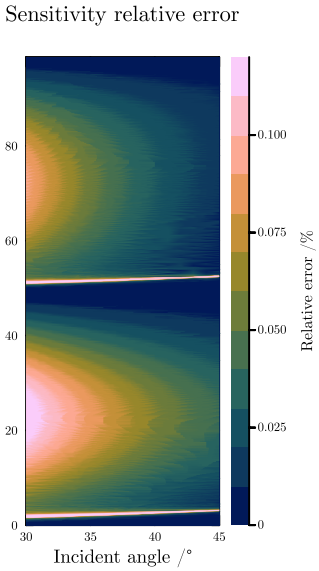

Fig. 10. Relative difference between the height sensitivity obtained with the proposed wavenumber-domain method and the range-dependent adjusted geometric approach discussed in the Appendix.

in the Appendix. We used the angle between the monostatic equivalent's line of sight and the normal to the surface as the incidence angle when computing the sensitivity with the geometric method. A different result, which is closer to the sensitivity obtained with the spectral method, is obtained when the complementary angle to the angle between the elevation direction $\hat{\boldsymbol{\xi}}$ and the normal to the surface is used as the incidence angle. We have defined this angle mathematically in (47). Fig. 10 shows the relative difference between the spectrally derived sensitivity and the sensitivity based on the geometric method, with the latter definition of the incidence angle.

IV. Discussion

The first two simulation scenarios act as tests to validate that the proposed wavenumber method for calculating the temporal lag and sensitivity produces sensible results. In the first scenario, we are testing the calculation of the temporal lag. Hence, we set up a Helix formation whose separation vector has a dominant along-track component, and a smaller radial component. In the baseline case, which is shown in the left panel of Fig. 6, we model both instruments as monostatic SARs with no squint. In this case, we expect to see the along-track baseline closely match the along-track separation of the formation and to have a small dependence on the range. If the second receiver operates bistatically, using the first instrument as a transmitter, then the along-track baseline

should be half the along-track separation. The results in Fig. 6 match these results.

In the second simulation scenario, we set up a Helix formation with a significant normal separation. Like the first scenario, we assume that the instruments operate monostatically and look in the zero-Doppler direction. Hence, we expect the spectrally derived sensitivity to agree with the expression for the sensitivity found in the literature. Fig. 7 shows that the results are in agreement with the conventional expression for the sensitivity.

We have verified that the wavenumber method agrees with the conventional expressions of along-track baseline and sensitivity for geometrically simple cases. We now move on to the more interesting case of a bistatic interferometer with an illuminator that leads the receivers by 350 km. The receivers are flying in a Helix formation with both an ascending node difference and an eccentricity difference. Thus, the separation of the receiving satellites varies in all three directions, the radial, the normal, and the tangential, sinusoidally with time.

Fig. 8 shows the temporal lag estimated using (31) on the left, and the geometric approximation on the right. Here, we are starting to see the two methods diverging. While a peak absolute difference of 0.40 ms might sound small, it is considerable when two SAR images need to be precisely aligned before processing is carried out to produce interferometric estimates. Furthermore, considerable effort was spent to have the geometrically calculated temporal lag approach the spectral temporal lag. Each satellite position and each incidence angle produce a unique ME system, for each of the two pairs of transmitter and the receiver.

The computationally cheaper and conceptually simpler approach of positioning the ME at the midpoint of the transmitter and the receiver, thus having a common ME position for all incidence angles at a given instance of time performs worse compared to the results presented in Fig. 8. The simpler geometric method overestimates the extremes of the temporal lag by 7 ms and misses its distribution with respect to time and range. In contrast to both variants of the geometric approach, the wavenumber method works for both monostatic and bistatic systems without requiring the calculation of virtual equivalent systems.

Fig. 9 illustrates the sensitivity to height of the same Helix formation in the left panel. The distribution of the values and the variation with time and incidence angle are in agreement between the two methods. There is a small but not insignificant difference in the magnitude of the sensitivity. The relative difference in the sensitivity estimated with the two methods is plotted in the right panel. The largest difference, which tends to 7% is in the near range and over the equator, which is where the normal separation of the formation also reaches its maximum.

During our experiments, we have found that changing the incidence angle used for the computation of the geometric sensitivity to the one defined by complementary angle to the angle between the elevation and the normal directions reduces the relative error between the spectral sensitivity and geometric sensitivity in scenarios that involve a complex formation, such as in the third scenario of Table I. Fig. 10 illustrates the improvement in the relative error, with a reduction of the maximum relative difference from 7% to 0.12% in the near range at equatorial latitudes, and a marked improvement throughout the domain. The latter definition of θ_i accounts for the fact that the line of sight and the elevation direction are not coplanar when the line of sight is squinted. The spectral method accounts for this directly by computing the wavenumber support difference along $\hat{\boldsymbol{\zeta}}$. Thus, making this adjustment to the geometric method brings the results closer to those obtained with the spectral method.

Furthermore, for both sensitivity calculations of scenario 3, we have scaled the expression of the sensitivity by the modulus of the bistatic line of sight. Whereas in a true monostatic system, the scaling factor would be equal to 2, in a bistatic system, the modulus of the line of sight is less than 2. The divergence of the modulus from 2 increases as the bistatic angle increases. Thus, in the ME of such an interferometer, the true modulus of the line of sight should be used. We discuss the line of sight modulus scaling factor and its effect on the results further in the Appendix.

We note to the reader that we were able to arrive at these modifications to the conventional expression of the sensitivity by iteratively experimenting with different adjustments and scaling factors. In light of this, the result of Fig. 10 serves as a cross-check of the geometric method against the spectral method. In configurations with larger bistatic angles or larger separations, the two methods diverge further.

The divergence stems from the fact that no monostatic system can capture the radiometric and interferometric properties of a bistatic system with sufficiently large baselines over different look angles and slow-time instants. As Fig. 1 shows, different look angles have different ME positions. Yet the difference between these positions is significantly larger than the distance that the satellite would travel in the time taken for the echoes of adjacent resolution cells to reach the instrument. Thus, the spectral method of calculating the temporal lag, spectral shift, and sensitivity to height is superior as it works regardless of the complexity of the separation between the two SARs or whether the system operates mono- or bistatically without the need for computing virtual systems and introducing scaling factors.

V. Conclusion

We have presented a method that uses the wavenumber support to compute the temporal lag and sensitivity of single-pass interferometers. Our method solves the problems that arise due to the difficulty of applying the ME approximation to interferometers with complex geometries. The proposed method accommodates both monostatic and bistatic interferometers without requiring adjustments to switch between the two. Furthermore, using the first-order linear expansion of the spectral support provides a simple system of equations that can be efficiently solved computationally.

Results from simulations show that for a Helix formation, the geometric method overestimates the temporal lag. Furthermore, the sensitivity estimated using the geometric method has a relative difference of up to 7% compared to the sensitivity estimated using the wavenumber method. Accurate knowledge of these parameters is necessary when designing XTIs to estimate the relative topography of dynamic surfaces, such as the ocean. Additionally, accurate knowledge of the temporal

lag and wavenumber shift between SAR surveys will benefit the processing of interferograms from future SAR missions that will feature squinted lines of sight and bistatic operation. The method is also useful for repeat-pass interferometry, as it allows the accurate computation of the reference orbits for processing. In the future, we aim to expand on this work by validating the method with an end-to-end simulation of SAR observables from a dynamic surface.

APPENDIX

A. Circular Complex Wide-Sense Stationary Processes and Their Frequency Components

To prove (17), we need to assume that the complex stochastic process $s(x)$ has a mean of zero, $\mathbb{E}\{s(x) = 0\}$, and that it is circular, that is, $\mathbb{E}\{s(x)s(u)\} = 0$. Thus, the second-order statistics of the process are encapsulated by the autocorrelation function

$$\mathbb{E}\{s(x)s(u)^*\} = R_s(x, u). \tag{39}$$

The following proof is an extension of [19, Th. 4] to continuous processes. The correlation of the Fourier transform of the stochastic process, $\tilde{s}(k_x)$, is

$$\begin{aligned}\mathbb{E}\{\tilde{s}(k)\tilde{s}(\kappa)^*\} &= \mathbb{E}\left\{\int s(x)e^{-jkx}\,\mathrm{d}x\left(\int s(u)e^{-j\kappa u}\,\mathrm{d}u\right)^*\right\}\\ &= \int\int \mathbb{E}\{s(x)s(u)^*\}e^{-jkx}\,\mathrm{d}x e^{j\kappa u}\,\mathrm{d}u\\ &= \int\int R_s(x-u)e^{-jkx}\,\mathrm{d}x e^{j\kappa u}\,\mathrm{d}u\\ &= \tilde{R}_s(k)\int e^{j(\kappa-k)u}\,\mathrm{d}u\\ &= \tilde{R}_s(k)\delta(k-\kappa)\end{aligned} \tag{40}$$

where the last equality follows from the definition of the delta function. Furthermore, since $s(x)$ is a circular complex process, then by Fourier inversion theorem $\tilde{s}(k_x)$ is also a circular complex process. Thus, the wavenumber components of $\tilde{s}(k_x)$ are uncorrelated.

B. Geometric Method for Calculating the Sensitivity

In the case of bistatic SAR where the transmitter has a position vector $\boldsymbol{r_t}$ and the receiver has position vector $\boldsymbol{r_r}$, the line of sight to a point on the surface $\boldsymbol{r_p}$ is

$$\boldsymbol{l_e} = \frac{\boldsymbol{r_t} - \boldsymbol{r_p}}{\|\boldsymbol{r_t} - \boldsymbol{r_p}\|} + \frac{\boldsymbol{r_r} - \boldsymbol{r_p}}{\|\boldsymbol{r_r} - \boldsymbol{r_p}\|}. \tag{41}$$

We define the ME as the system that would observe a given point with the same line of sight as the bistatic SAR. Thus, the line of sight of the ME is parallel to $\boldsymbol{l_e}$. We position the ME at the intersection of the line that starts at $\boldsymbol{r_p}$ and follows $\boldsymbol{l_e}$, and the line segment that connects the transmitter and the receiver. Thus, we can find the position of the monostatic equivalent by solving the following system of equations

$$\boldsymbol{r_p} + s\boldsymbol{l_e} = \boldsymbol{r_t} + q(\boldsymbol{r_r} - \boldsymbol{r_t}) \tag{42}$$

where s and q are the unknowns to solve for.

$\boldsymbol{r_p}$ varies with look angle and time, while the positions of the transmitter and the receiver vary with time only. Thus, (42) has a unique solution for each combination of look angle and time. Consequently, each resolution cell in the SAR signal will have a corresponding pair of monostatic equivalents, one for each receiver.

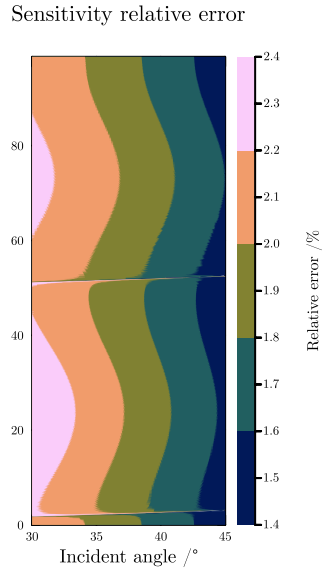

Fig. 11. Relative error of the sensitivity calculated using the wavenumber method with respect to the conventional sensitivity expression. For the expression of the sensitivity, the incidence angle is computed according to (47) and the scaling of the wavelength described in (46) is omitted. A scaling factor of 2, corresponding to a monostatic system, is used instead.

Once the two MEs for a given resolution cell are found, the relative position vector of the two equivalent systems is vector of the two equivalent systems is

$$\Delta\boldsymbol{r_e} = \boldsymbol{r_{e2}} - \boldsymbol{r_{e1}} \tag{43}$$

where $\boldsymbol{r_{e2}}$ is the position of the equivalent system of the transmitter with the second receiver, and $\boldsymbol{r_{e1}}$ that of the transmitter with the first receiver. We use the relative position of the equivalent systems to calculate the effective along-track baseline [18]

$$B_\parallel = -\Delta\boldsymbol{r}_{\boldsymbol{e}_T} + \Delta\boldsymbol{r}_{\boldsymbol{e}_N}\frac{\boldsymbol{l}_{\boldsymbol{e}_T}}{\boldsymbol{l}_{\boldsymbol{e}_N}} \tag{44}$$

where the subscripts T and N denote the tangential and the normal component of the vector, respectively. The temporal lag between acquisitions is equal to the effective along-track baseline divided by the flight speed of the satellite.

The perpendicular baseline of the interferometer is

$$B_\perp = \Delta\boldsymbol{r_c} \cdot \hat{\boldsymbol{\xi}} \tag{45}$$

where $\Delta\boldsymbol{r_c} = (\Delta\boldsymbol{r}_{\boldsymbol{e}_N}\boldsymbol{l}_{\boldsymbol{e}_T}/\boldsymbol{l}_{\boldsymbol{e}_N}, \Delta\boldsymbol{r}_{\boldsymbol{e}N}, \Delta\boldsymbol{r}_{\boldsymbol{e}R})^T$ is the relative position after shifting the two equivalent systems to align their lines of sight. We use the perpendicular baseline to calculate the sensitivity to height of the interferometer using the conventional relation [4], [5]

$$\frac{\partial\phi}{\partial h} = \frac{2\pi\|\boldsymbol{l_e}\|B_\perp}{\lambda_0 R_s \sin\theta_i} \tag{46}$$

where in this case the slant range R_s is equal to the slant range from the position of the ME to the resolution cell and the incidence angle θ_i is the angle formed by the bistatic line of sight and the normal to the surface.

The careful reader would have noticed that the sensitivity is scaled by the modulus of the bistatic line of sight. It effectively scales the wavelength by the inverse of the modulus of the bistatic line of sight. The scaling arises because the modulus of the bistatic line of sight is smaller than the modulus of the monostatic line of sight. While the monostatic, two-way line of sight has a modulus of 2, the bistatic line of sight is smaller than that by the cosine of half the bistatic angle. The smaller modulus scales the wave vector. Hence, where the monostatic wave vector would have a modulus of $2\,k_0$, the bistatic wave vector would have a modulus of $\|\hat{\boldsymbol{l}}_{\boldsymbol{T}_i} + \hat{\boldsymbol{l}}_{\boldsymbol{R}_i}\|k_0$, effectively scaling the wavenumber, thus the wavelength.

An alternative choice for the incidence angle is to calculate it based on the elevation vector and the normal to the surface

$$\theta_i = \arcsin\left(\hat{\boldsymbol{\xi}} \cdot \hat{\boldsymbol{n}}\right). \tag{47}$$

The two definitions of θ_i are congruent for a monostatic system with a line of sight in the zero-Doppler direction.

Fig. 11 shows the relative difference between the spectrally derived sensitivity and the sensitivity obtained with the geometric method according to (46). For this result, we replaced $\|\boldsymbol{l}_{\boldsymbol{e}}\|$ by 2 and used (47) for θ_i. Comparing the results with Fig. 10 shows that ignoring the scaling due to the bistatic wave vector, and instead modeling the system as a monostatic interferometer, produces a markedly less accurate result.

REFERENCES

[1] H. C. Graber, D. R. Thompson, and R. E. Carande, "Ocean surface features and currents measured with synthetic aperture radar interferometry and HF radar," *J. Geophys. Res., Oceans*, vol. 101, no. 11, pp. 25813–25832, Nov. 1996.

[2] R. M. Goldstein, T. P. Barnett, and H. A. Zebker, "Remote sensing of ocean currents," *Science*, vol. 246, no. 4935, pp. 1282–1285, 4935.

[3] R. M. Goldstein and H. A. Zebker, "Interferometric radar measurement of ocean surface currents," *Nature*, vol. 328, pp. 707–709, Aug. 1987.

[4] R. Bamler and P. Hartl, "Synthetic aperture radar interferometry," *Inverse Problems*, vol. 14, no. 4, pp. 1–54, Aug. 1998.

[5] H. A. Zebker and R. M. Goldstein, "Topographic mapping from interferometric synthetic aperture radar observations," *J. Geophys. Res.*, vol. 91, no. 5, pp. 4993–4999, Apr. 1986.

[6] F. Gatelli, A. Monti Guamieri, F. Parizzi, P. Pasquali, C. Prati, and F. Rocca, "The wavenumber shift in SAR interferometry," *IEEE Trans. Geosci. Remote Sens.*, vol. 32, no. 4, pp. 855–865, Jul. 1994.

[7] R. Bamler and G. W. Davidson, "Multiresolution signal representation for phase unwrapping and interferometric SAR processing," in *Proc. IEEE Int. Geosci. Remote Sens. Symp. Remote Sens. Scientific Vis. Sustain. Develop.*, Aug. 1997, pp. 865–868.

[8] C. Prati and F. Rocca, "Improving slant-range resolution with multiple SAR surveys," *IEEE Trans. Aerosp. Electron. Syst.*, vol. 29, no. 1, pp. 135–143, 1993.

[9] G. Krieger et al., "TanDEM-X: A satellite formation for high-resolution SAR interferometry," *IEEE Trans. Geosci. Remote Sens.*, vol. 45, no. 11, pp. 3317–3341, Nov. 2007.

[10] P. López-Dekker, H. Rott, P. Prats-Iraola, B. Chapron, K. Scipal, and E. D. Witte, "Harmony: An Earth explorer 10 mission candidate to observe land, ice, and ocean surface dynamics," in *Proc. IEEE Int. Geosci. Remote Sens. Symp. (IGARSS)*, Jul. 2019, pp. 8381–8384.

[11] D. D'Aria, A. M. Guarnieri, and F. Rocca, "Focusing bistatic synthetic aperture radar using dip move out," *IEEE Trans. Geosci. Remote Sens.*, vol. 42, no. 7, pp. 1362–1376, Jul. 2004.

[12] R. Wu and M. N. Toksöz, "Diffraction tomography and multisource holography applied to seismic imaging," *Geophysics*, vol. 52, no. 1, pp. 11–25, Jan. 1987.

[13] S. Tebaldini and F. Rocca, "Multistatic wavenumber tessellation: Ideas for high resolution P-band SAR missions," in *Proc. IEEE Int. Geosci. Remote Sens. Symp. (IGARSS)*, Jul. 2017, pp. 2412–2415.

[14] D. Nahamoo, S. X. Pan, and A. C. Kak, "Synthetic aperature diffraction tomography and its interpolation-free computer implementation," *IEEE Trans. Sonics Ultrason.*, vol. SU-31, no. 4, pp. 218–229, Jul. 1984.

[15] S. Tebaldini, M. Manzoni, L. Ferro-Famil, F. Banda, and D. Giudici, "FDM MIMO spaceborne SAR tomography by minimum redundancy wavenumber illumination," *IEEE Trans. Geosci. Remote Sens.*, vol. 62, pp. 1–19, 2024, Art. no. 5207119, doi: 10.1109/TGRS.2024.3371267.

[16] P. Lopez-Dekker, P. Prats, F. De Zan, D. Schulze, G. Krieger, and A. Moreira, "TanDEM-X first DEM acquisition: A crossing orbit experiment," *IEEE Geosci. Remote Sens. Lett.*, vol. 8, no. 5, pp. 943–947, Sep. 2011.

[17] S. D'Amico and O. Montenbruck, "Proximity operations of formation-flying spacecraft using an eccentricity/inclination vector separation," *J. Guid., Control, Dyn.*, vol. 29, no. 3, pp. 554–563, May 2006.

[18] A. Theodosiou, M. Kleinherenbrink, and P. López-Dekker, "Wide-swath ocean altimetry using multisatellite single-pass interferometry," *IEEE Trans. Geosci. Remote Sens.*, vol. 61, pp. 1–21, 2023, Art. no. 5210721, doi: 10.1109/TGRS.2023.3287675.

[19] F. D. Neeser and J. L. Massey, "Proper complex random processes with applications to information theory," *IEEE Trans. Inf. Theory*, vol. 39, no. 4, pp. 1293–1302, Jul. 1993.

Andreas Theodosiou was born in Nicosia, Cyprus, in 1993. He received the B.A. and M.Eng. degrees in electrical and information sciences from the University of Cambridge, Cambridge, U.K., in 2018. He is currently pursuing the Ph.D. degree in synthetic aperture radar (SAR) with the Delft University of Technology, Delft, The Netherlands.

From 2018 to 2019, he was with the RF Payloads Section, European Space Agency, Noordwijk, The Netherlands. In 2019, he joined the Faculty of Civil Engineering and Geoscience, Delft University of Technology, Delft, The Netherlands, to work on performance models for the Earth Explorer 10 Mission, Harmony. His research interests include future SAR mission concepts and ocean remote sensing.

Paco López-Dekker (Senior Member, IEEE) was born in Nijmegen, The Netherlands, in 1972. He received the Ingeniero degree in telecommunication engineering from the Universitat Politècnica de Catalunya (UPC), Barcelona, Spain, in 1997, the M.S. degree in electrical and computer engineering from the University of California at Irvine, Irvine, CA, USA, in 1998, under the Balsells Fellowship, and the Ph.D. degree in clear-air imaging radar systems to study the atmospheric boundary layer from the University of Massachusetts, Amherst, MA, USA, in 2003.

In 2003, he joined Starlab Barcelona, Barcelona, where he worked on the development of Global Navigation Satellite Systems Reflectometry (GNSS-R) sensors and techniques. From 2004 to 2006, he was a Visiting Professor with the Department of Telecommunications and Systems Engineering, Universitat Autònoma de Barcelona, Bellaterra, Spain. From November 2009 to August 2016, he led the SAR Missions Group, Microwaves and Radar Institute, German Aerospace Center, Weßling, Germany. Since September 2016, he has been an Associate Professor with the Geoscience and Remote Sensing Department, Faculty of Civil Engineering and Geosciences, Delft University of Technology, Delft, The Netherlands. He has been deeply involved in the development of several radar missions and mission proposals and is the Lead Investigator of the Harmony European Space Agency (ESA) Earth Explorer 10 Mission. He has coauthored over 50 peer-reviewed journal articles and more than 125 conference contributions in a broad range of topics related to radar remote sensing.

Dr. López-Dekker was awarded a Ramon y Cajal Grant to conduct pioneering research on bistatic synthetic aperture radar (SAR) at the Remote Sensing Laboratory, UPC, In March 2006.